

Influence of Filler Alloy Composition and Process Parameters on the Intermetallic Layer Thickness in Single-Sided Cold Metal Transfer Welding of Aluminum-Steel Blanks



ZAHRA SILVAYEH, RUDOLF VALLANT, CHRISTOF SOMMITSCH,
BRUNO GÖTZINGER, WERNER KARNER, and MATTHIAS HARTMANN

Hybrid components made of aluminum alloys and high-strength steels are typically used in automotive lightweight applications. Dissimilar joining of these materials is quite challenging; however, it is mandatory in order to produce multimaterial car body structures. Since especially welding of tailored blanks is of utmost interest, single-sided Cold Metal Transfer butt welding of thin sheets of aluminum alloy EN AW 6014 T4 and galvanized dual-phase steel HCT 450 X + ZE 75/75 was experimentally investigated in this study. The influence of different filler alloy compositions and welding process parameters on the thickness of the intermetallic layer, which forms between the weld seam and the steel sheet, was studied. The microstructures of the weld seam and of the intermetallic layer were characterized using conventional optical light microscopy and scanning electron microscopy. The results reveal that increasing the heat input and decreasing the cooling intensity tend to increase the layer thickness. The silicon content of the filler alloy has the strongest influence on the thickness of the intermetallic layer, whereas the magnesium and scandium contents of the filler alloy influence the cracking tendency. The layer thickness is not uniform and shows spatial variations along the bonding interface. The thinnest intermetallic layer (mean thickness $< 4 \mu\text{m}$) is obtained using the silicon-rich filler Al-3Si-1Mn, but the layer is more than twice as thick when different low-silicon fillers are used.

DOI: 10.1007/s11661-017-4277-5

© The Author(s) 2017. This article is an open access publication

I. INTRODUCTION

REDUCING the vehicle weight to improve fuel efficiency and simultaneously increasing the passenger's safety are unbroken trends in the modern automotive industry. Particularly high-strength steels, *e.g.*, dual phase (DP), transformation-induced plasticity (TRIP), and twinning-induced plasticity (TWIP) steel grades^[1,2] as well as aluminum (Al) alloys, *e.g.*, series AW 5xxx and AW 6xxx,^[3-5] play important roles in innovative multimaterial car body design. In order to benefit from the specific advantages of each of these material groups

and to obtain car bodies offering both high safety and low weight, joining of aluminum alloys with steels is mandatory.^[6] Various processes for mechanical joining, adhesive bonding, brazing, and welding of dissimilar metal sheets in the automotive industry were developed.^[6-8] Basically, two main welding process categories are distinguished: solid-state welding and fusion welding, both including various subcategories.^[9-11] An opportunity for joining particularly thin metal sheets by combining the advantages of both fusion and solid-state welding offers the Cold Metal Transfer (CMT) process developed by Fronius.^[12] The CMT process enables spatter-free joining of similar metals, *e.g.*, Al-Al bead-on-plate^[13-15] or butt welding,^[16] as well as joining of dissimilar metals, *e.g.*, Al-steel butt welding with tapered steel sheet edges,^[17-19] overlap welding,^[20-29] or even spot welding.^[30-32] In comparison with conventional gas metal arc (GMA) welding processes, the heat input of the CMT process is significantly reduced. Since both the aluminum-based sheet and the filler melt whereas the steel sheet remains solid, joining is achieved by the combination of aluminum welding and steel brazing.^[17-21]

ZAHRA SILVAYEH, RUDOLF VALLANT, and CHRISTOF SOMMITSCH are with the Graz University of Technology, Institute of Materials Science, Joining and Forming (IMAT), Kopernikusgasse 24/I, 8010 Graz, Austria. Contact e-mail: zahra.silvayeh@tugraz.at
BRUNO GÖTZINGER and WERNER KARNER are with the Magna Steyr Engineering Austria AG & Co KG and Magna Steyr Fahrzeugtechnik AG & Co KG, Liebenauer Hauptstraße 317, 8041 Graz, Austria. MATTHIAS HARTMANN is with the Austrian Institute of Technology (AIT), Light Metals Technologies Ranshofen GmbH (LKR), P.O. Box 26, 5282 Ranshofen, Austria.

Manuscript submitted January 13, 2017.

Article published online August 16, 2017

However, welding of aluminum alloys with steels still remains challenging, because aluminum (Al) and iron (Fe) exhibit different chemical and physical properties and a brittle intermetallic (IM) layer, mainly consisting of Al_xFe_y phases, may excessively form at the interface between these materials.^[10,11,33,34] The IM layer which forms between the aluminum weld and the steel sheet ensures dissimilar bonding, but limiting its thickness is mandatory for obtaining ductile joints for both static and dynamic applications.^[20,21] Among the Al_xFe_y phases listed in the binary Al-Fe phase diagram,^[35] two main phases were identified in laboratory experiments to form at the interface between solid iron or steel and liquid aluminum or its alloys: Al_5Fe_2 as the major η -phase^[36–38] together with Al_3Fe (also referred to as $Al_{13}Fe_4$) as the minor θ -phase.^[39–55] Both^[17–19,21,24,27,29] or at least either one^[22, 23] of these two phases were also found to form during dissimilar CMT welding of aluminum alloys with steel. These experimental studies also show that the interfaces are typically tongue-like between Al_5Fe_2 and steel, whereas they are finely serrated between Al_3Fe and aluminum. In multicomponent systems, formation, thickness, and morphology of the IM layer are influenced by different alloying elements or impurities, respectively.^[56] Several studies revealed that in particular silicon (Si) additions to aluminum melts decelerate the growth and reduce the thickness of the IM layer forming on steel samples hot dipped into the melts.^[36,40,51–54] The same effect was observed in dissimilar welding of aluminum alloys with steel using Al-Si-based fillers.^[10,19,57] Although the influence of silicon on the growth of the IM layer is still not completely understood, it is assumed that the diffusivity of aluminum atoms in the solid Al_5Fe_2 phase is significantly reduced due to the occupation of vacancy sites by silicon atoms,^[40,52] or that silicon reduces the activity coefficient of aluminum atoms in iron at the Al-Fe interface.^[56]

The main objective of this study was to investigate the influences of different filler alloy compositions and process parameters on the thickness of the IM layer. The current study also demonstrates that butt welds between aluminum alloy and steel sheets were successfully produced with the single-sided CMT process without tapering the sheet edges before welding.^[58]

II. EXPERIMENTAL

A. Materials

In the current study, 1.15-mm-thick sheets of aluminum alloy EN AW 6014 T4 were joined with 0.80-mm-thick sheets of galvanized dual-phase steel HCT 450 X + ZE 75/75. The sheet dimensions were approximately 250 mm × 150 mm. The zinc (Zn) coating of the steel sheets was 7.5 μ m thick. However, the cutting edges were uncoated, since the sheets were cut from a hot-dipped galvanized coil. Six different aluminum-based filler wires (\varnothing 1.20 mm) designated with code letters A, B, C, D, E, F, and G were tested. The nominal chemical compositions of these

Table I. Nominal Chemical Compositions^[59] of the Base Metal Sheets (St, Al), of the Commercial Filler Alloys (A–D), and of the Self-Produced Filler Alloys (E–G) in wt pct

Code	Material	Mg	Mn	Si	Fe	Cu	Zn	Ti	Cr	V	C	P	S	B	Zr	Sc	Al
St	1.0937 (HCT 450 X)		max. 2.0	max. 0.8	bal.			Ti+Nb <0.15	Cr+Mo <0.1	max. 0.2	max. 0.14	max. 0.08	max. 0.015	max. 0.005			max. 2.0
Al	EN AW 6014	0.4-0.8	0.05-0.2	0.3-0.6	max. 0.35	max. 0.25	max. 0.1	max. 0.1	max. 0.2	0.05-0.2							bal.
A	EN AW 5183	4.3-5.2	0.5-1.0	max. 0.4	max. 0.4	max. 0.1	max. 0.25	max. 0.15	0.05-0.25								bal.
B	EN AW 5087	4.5-5.2	0.7-1.1	max. 0.25	max. 0.4	max. 0.05	max. 0.25	max. 0.15	0.05-0.25						0.1-0.2		bal.
C	EN AW 6082	0.6-1.2	0.4-1.0	0.7-1.3	max. 0.5	max. 0.1	max. 0.2	max. 0.1	max. 0.25								bal.
D	Al-3Si-1Mn	max. 0.01	0.8-1.2	2.5-3.5	max. 0.2	max. 0.03		max. 0.005	max. 0.01								bal.
E	Al-4Mg-0.6Sc	3.5-4.0	0.05-0.08													0.55-0.6	bal.
F	Al-0.3Mg-0.5Sc-0.4Zr	0.2-0.3	0.03-0.05	0.03-0.05	0.02-0.04										0.3-0.5	0.4-0.6	bal.
G	Al-0.3Mg-0.4Sc-0.3Zr	0.2-0.3	0.03-0.05	0.03-0.05	0.02-0.04										0.2-0.3	0.3-0.5	bal.

materials are summarized in Table I. Commercial fillers A-D are typically used for industrial welding applications, whereas fillers E-G were specially produced for the experiments. Filler D was recommended for obtaining optimized mechanical properties of aluminum-steel joints produced with CMT welding.^[19] Filler alloys E-G contained scandium (Sc), which is known as effective grain refiner reducing the hot-cracking susceptibility during solidification of aluminum alloys, *e.g.*, in casting or welding.^[60-64] These effects were experimentally observed in autogenous gas tungsten arc (GTA) welding of AA 7108 alloy containing scandium,^[65] as well as in metal inert gas (MIG) welding of AA 7050 aerospace alloy^[66] and CMT welding of EN AW 6014 automotive alloy^[68] when using scandium-containing filler wires. Experiments simulating weld bead solidification by wedge-shaped casting of scandium-containing AA 2024 and AA 7475 aerospace alloys also confirm the positive effects of scandium on the microstructure.^[67]

B. Welding Process

The dissimilar metal sheets were joined with the single-sided Cold Metal Transfer welding process using a Fronius CMT Advanced 4000 power source. The welding torch was mounted on a KUKA KR 30-2

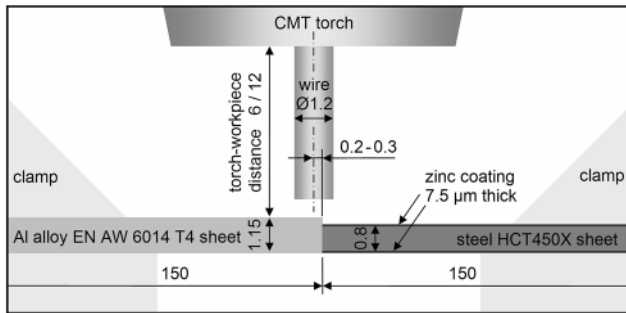


Fig. 1—Schematic illustration of the welding configuration (dimensions in mm).

robot. Two different torch types, the Fronius CMT Braze+ torch and the Fronius Robacta500 torch with a torch-body angle of 22 deg, were tested. Two different vertical distances between the welding torches and the workpiece, 6 and 12 mm, were applied. The metal sheets were clamped without overlapping in horizontal butt welding configuration, as illustrated schematically in Figure 1. Prior to welding, the surfaces of the sheets were cleaned with isopropanol.

The experimental welding process parameters are summarized in Table II. All experiments were performed with the constant welding speed of 0.4 m/min using the shielding gas argon (Ar) at a flow rate of 12 l/min. Based on the welding speed, v (m/min), the mean welding current, I (A), and the mean welding voltage, U (V), the nominal heat input, E (J/mm), is calculated as

$$E = 0.06 \frac{UI}{v}. \quad [1]$$

However, since both I and U are fluctuating quantities and due to electrical and thermal losses, the effective heat input into the weld is definitely lower than the nominal heat input E . The wire feed rate, w (m/min), has to be increased with the increasing nominal heat input in order to add sufficient filler alloy to the weld bead. As illustrated by the line fit in Figure 2, the relationship between E and w was almost linear in the experiments conducted in this study.

C. Metallographic Investigations

The samples were cut perpendicular to the welding direction in order to investigate the microstructure of the weld seam's cross section. After cold-embedding of the samples into epoxy resin, grinding with sand papers and polishing with diamond suspensions were performed using a semi-automated machine. Macroscopic images of the weld seam were captured using a Zeiss SteREO Discovery.V20 microscope equipped with a Zeiss AxioCam ICc5 camera. The microstructures of the

Table II. Welding Process Parameters

Sample	Filler Alloy	Torch Type	d (mm)	w (m/min)	U (V)	I (A)	E (J/mm)
05	EN AW 5183	CMT Braze+	6	3.7	8.0	69	83
06	EN AW 5183	CMT Braze+	12	3.7	8.0	69	83
07	EN AW 5183	Robacta500	12	4.1	8.2	74	91
09	EN AW 5087	CMT Braze+	6	4.7	9.3	68	95
10	EN AW 5087	CMT Braze+	12	3.4	7.9	66	78
08	EN AW 5087	Robacta500	12	3.9	8.1	71	86
12	EN AW 6082	CMT Braze+	6	3.6	8.0	68	82
11	EN AW 6082	CMT Braze+	12	3.8	8.1	70	85
13	EN AW 6082	Robacta500	12	3.9	8.1	71	86
14	Al-3Si-1Mn	CMT Braze+	6	3.7	8.0	69	83
15	Al-3Si-1Mn	CMT Braze+	12	3.7	8.0	69	83
16	Al-3Si-1Mn	Robacta500	12	3.9	8.1	71	86
17	Al-4Mg-0.6Sc	CMT Braze+	6	3.7	8.0	69	83
18	Al-4Mg-0.6Sc	CMT Braze+	12	3.9	8.1	71	86
19	Al-4Mg-0.6Sc	Robacta500	12	4.1	8.2	74	91
20	Al-0.3Mg-0.5Sc-0.4Zr	CMT Braze+	6	4.0	8.1	73	89
22	Al-0.3Mg-0.4Sc-0.3Zr	CMT Braze+	6	3.9	8.1	71	86

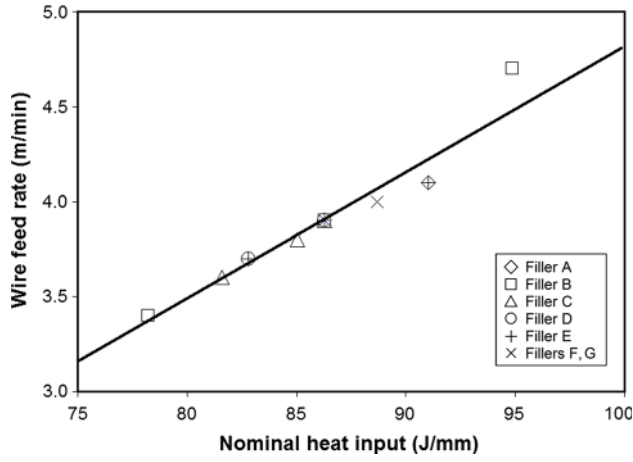


Fig. 2—Relationship between the nominal heat input and the wire feed rate.

weld seam and of the IM layer between the steel sheet and the weld seam were investigated using a Zeiss Axio Observer.Z1m microscope equipped with a Zeiss Axio-Cam MRC5 camera. The thickness of the IM layer was measured using the microscope-software Zeiss AxioVision SE64. The chemical compositions of the IM layers of samples 20 and 22 were detected using two scanning electron microscopes (SEM) equipped with energy-dispersive X-ray (EDX) systems: a FEI ESEM Quanta 200 SEM with an EDAX Genesis EDX system for the spot scans, and a Zeiss LEO 1450VP SEM with a Bruker AXS QUANTAX 400 EDX system and a XFlash[®] 4010 detector for the line scans, both operated with an acceleration voltage of 15 kV. For each of the welding experiments, one joint cross section was investigated. The positions for measuring the thickness of the IM layer were randomly selected along the bonding interface between the weld seam and the steel sheet. Needle-shaped IM particles protruding from the continuous banded layer were not considered. The method of thickness measurement is schematically illustrated in Figure 3(a), and some of the thickness values measured with the optical microscope are exemplarily shown in Figure 3(b).

D. Calculating the Mean Layer Thickness

Selected local thickness maxima, as approximated with the dotted envelope in Figure 3(a), were then considered for calculating the mean thickness. Based on x_t , x_s , and x_b , the measured values at the top section, the side section, and the bottom section of the bonding interface, the mean layer thicknesses per section, \bar{x}_{top} , \bar{x}_{side} and \bar{x}_{bottom} , as well as the mean layer thickness per sample, \bar{x} , were calculated:

$$\bar{x}_{top} = \frac{1}{25} \sum_{t=1}^{25} x_t, \quad \bar{x}_{side} = \frac{1}{10} \sum_{s=1}^{10} x_s, \quad \bar{x}_{bottom} = \frac{1}{25} \sum_{b=1}^{25} x_b, \quad [2]$$

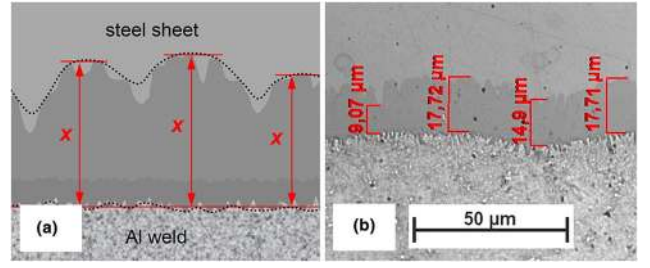


Fig. 3—Schematic illustration of the thickness measurement method (a) and examples of measured values (b).

$$\bar{x} = \frac{1}{60} \left(\sum_{t=1}^{25} x_t + \sum_{s=1}^{10} x_s + \sum_{b=1}^{25} x_b \right) \quad [3]$$

It should be noted that Eqs. [2] and [3] provide rather approximations than exact values of the mean thicknesses, because diffuse boundaries, strongly fragmented layer interfaces, or layers being thinner than 1 μm make the measurement of the IM layer thickness difficult. Nevertheless, the mean thickness value calculated from the measured values represents a simple and effective criterion for comparing the impacts of different parameters on the actual IM layer thickness.

III. RESULTS

The aluminum alloy sheets and the steel sheets were successfully joined with each of the filler alloys tested. Although the fillers were just added from a single side, the final weld seams penetrate the blanks completely, and the weld surfaces show neither spatter nor macroscopic defects. However, the weld seams contained internal defects such as gas pores or hot cracks, which are discussed elsewhere.^[68] Optical microscopy analysis revealed that local melting of the aluminum alloy sheet occurred in the region close to the weld seam, but the steel sheet remained solid, as shown exemplarily in Figures 4(a) and (d). Hence, bonding between the steel and the weld seam was just achieved by the IM layer.

A. Structure of the Intermetallic Layer

The SEM-EDX analysis conducted exemplarily on samples 20 and 22 indicated that the IM layer consists of two sublayers, most probably the Al_5Fe_2 phase close to the steel surface and the Al_3Fe phase penetrating the weld. This result is also confirmed by previous CMT welding experiments.^[17–19,21,24,27,29] The positions of the EDX spot scans on sample 20 are visualized in Figures 4(c) and (f); the spot scan results are summarized in Table III. It should be noted that a comparatively high aluminum concentration was detected at position 4, because this position was located close to the aluminum-rich weld. Figures 4(b) and (e) show both the

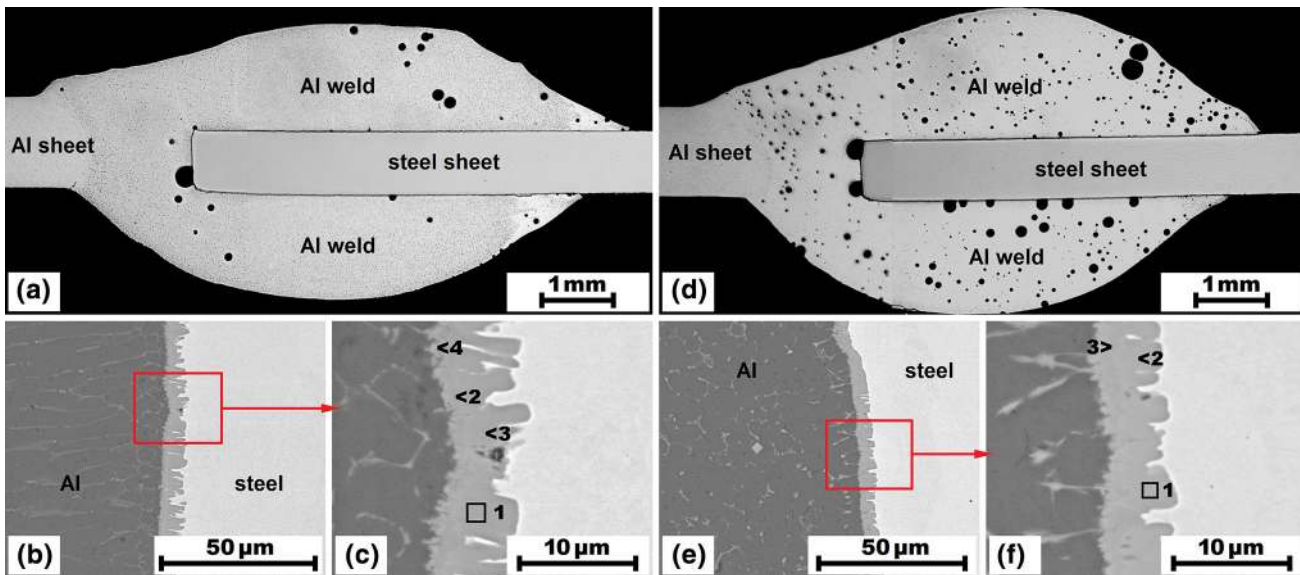


Fig. 4—Merged optical micrographs of the joint cross sections of sample 20 (a) and sample 22 (d). Detailed SEM-EDX images of the IM layer (b), (e); and positions of the SEM-EDX spot scans (c), (f).

Table III. Results of the SEM-EDX Spot Analysis

Sample	Pos.	Al (at. pct)	Fe (at. pct)	Al:Fe	Phase
20	1	72.13	27.87	2.59	Al_5Fe_2
20	2	73.78	26.22	2.81	Al_3Fe
20	3	71.85	28.15	2.55	Al_5Fe_2
20	4	81.74	18.26	4.48	$Al_3Fe + Al$
22	1	69.19	30.81	2.25	Al_5Fe_2
22	2	70.95	29.05	2.44	Al_5Fe_2
22	3	74.93	25.07	2.99	Al_3Fe

typical finger-/tongue-like interface between Al_5Fe_2 and the steel sheet as well as the finely serrated interface between Al_3Fe and the weld.

Figures 5(a) and (d) show typical IM layers of sample 20 captured using the SEM. The positions of the corresponding SEM-EDX line scans across the IM layers are shown in Figures 5(b) and (e). The line scan graphs, Figures 5(c) and (f), demonstrate qualitatively that the local aluminum content decreases with the increasing iron content. In particular, this becomes obvious with a closer look at Figure 5(f), where the locations of the three distinct aluminum peaks are identical with the locations of the three iron valleys, as indicated by the arrow markings.

B. Influence Parameters on the Layer Thickness

It is commonly known that increasing the heat input promotes the growth of the IM layer, because the growth is mainly controlled by diffusion, which enhances with increasing temperature.^[69] This was also observed in recent CMT welding of aluminum alloy A 6061 T6 with galvanized steel DP 800 using the filler alloy Al-3Si-Mn^[70] and in CMT weld deposition of

filler alloy A 4043 (Al-5Si) onto galvanized steel S235.^[71] The results of the current study confirm this trend: the mean thickness of the IM layer, \bar{x} , tends to increase with heat input, E , as illustrated by the ascending trend line in Figure 6. It must be pointed out that this line visualizes the general trend taking into account \bar{x} from all experiments conducted. However, excessive scattering of the points in the diagram indicates that additional parameters influencing \bar{x} exist. The mean thicknesses of the IM layer determined for samples 05-22 depending on (i) the filler alloy used for welding; (ii) the torch type, CMT Braze+ or Robacta500; and (iii) the distance between the torch and the workpiece, 6 or 12 mm, are shown in Figure 7. In the following, the influences of these parameters on the formation of the IM layer are discussed in detail.

C. Influence of the Filler Alloy Composition

Figure 8 shows the microstructures of two joints produced by means of the silicon-containing fillers Al-3Si-1Mn and EN AW 6082, respectively. The thinnest IM layer of $\bar{x} < 4 \mu m$ is formed when filler Al-3Si-1Mn was used in combination with the CMT Braze+ torch (samples 14 and 15). Thin IM layers of $\bar{x} \approx 5 \mu m$ were also formed when filler EN AW 6082 was used (samples 11-13). The comparatively high silicon contents in both these filler alloys confirm the well-known phenomenon: silicon generally inhibits the formation of the IM layer. However, both polyhedral and isolated needle-shaped IM particles (samples 14 and 15) as well as dense clusters of comparatively long needle-shaped IM particles (sample 16) were observed next to the IM layer when filler Al-3Si-1Mn was used. The detailed investigation of the cross sections of samples 14 and 16, Figures 8(a) and (f), revealed that

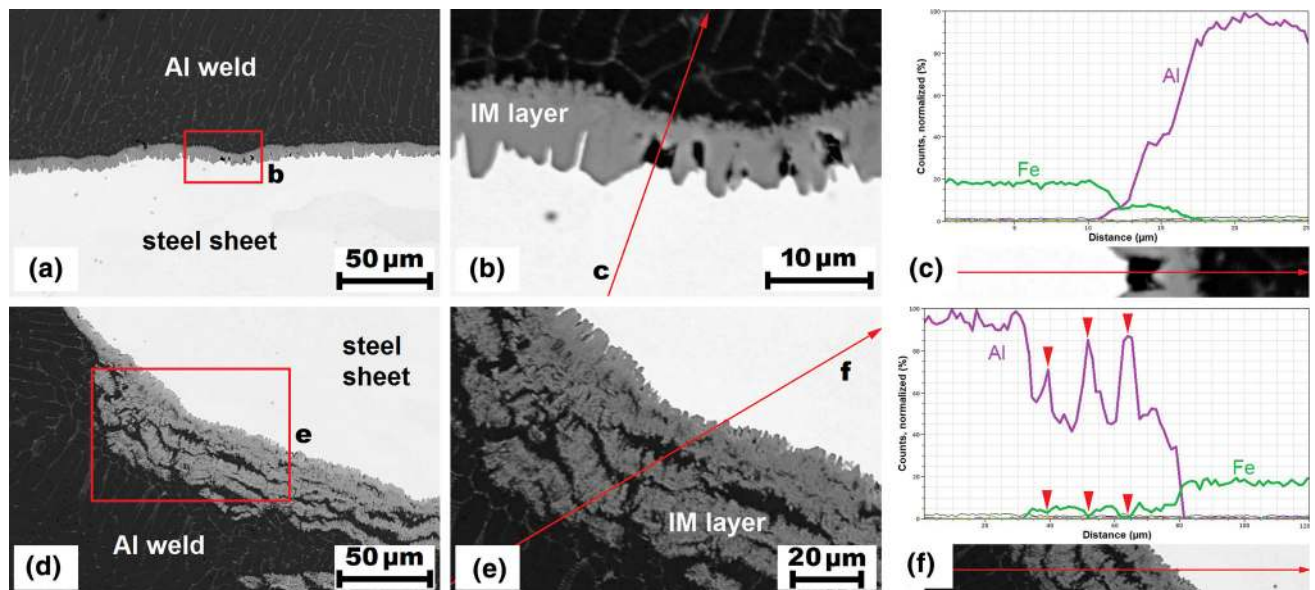


Fig. 5—Details of sample 20 captured with the SEM. Typical single-banded IM layer (a), multibanded IM layer at the bottom edge of the steel sheet (d); positions of the SEM-EDX line scans (b), (e); and qualitative line scan graphs redrawn for Al and Fe (c), (f).

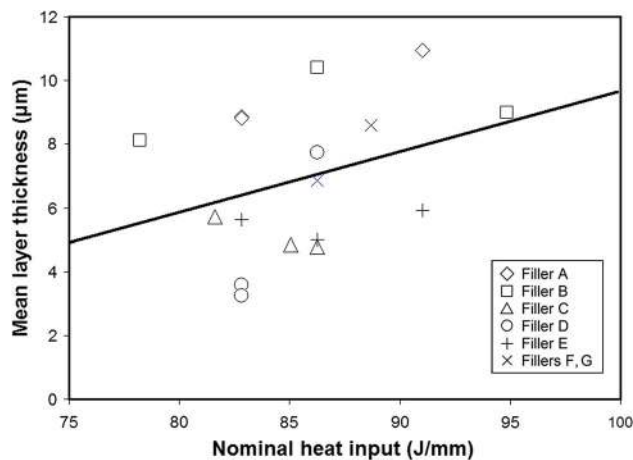


Fig. 6—Relationship between the nominal heat input and the mean thickness of the IM layer.

the needle-shaped particles occurred predominantly at the top section of the bonding interface. The microstructure details of Figures 8(g) through (j) illustrate that the faceted particles in sample 16 are up to several hundred micrometers in length, but their lengths decrease until they completely disappear at the cutting edge of the steel sheet. The faceted needle-shaped morphology is typical for some ternary Al-Fe-Si phases,^[72,73] which may form if iron or aluminum atoms in Al_xFe_y phases are partially substituted by silicon atoms during weld bead solidification.^[57] This kind of substitution also may cause the formation of particles with the faceted polyhedral morphology occurring in sample 14, as exemplarily marked in Figures 8(b) and (e).^[18,19]

The thickness of the IM layer was distinctly influenced by the silicon content of the filler alloys, but the experiments did not give clear indications about the

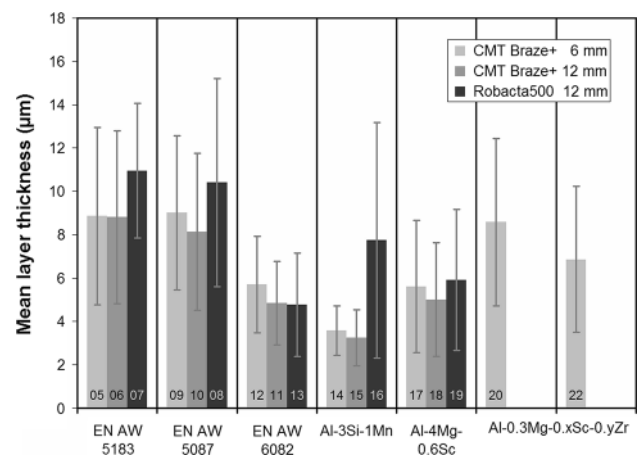


Fig. 7—Mean thicknesses of the IM layer determined for samples 05-22 welded with different filler alloys and torch types.

effect of the magnesium (Mg) content. Thick IM layers of $\bar{x} > 8 \mu\text{m}$ formed when using the magnesium-rich fillers, EN AW 5183 and EN AW 5087 (samples 05–10), containing about 5 wt pct magnesium, but also when using the magnesium-poor filler Al-0.3Mg-0.5Sc-0.4Zr (sample 20). Medium IM layers of $\bar{x} \approx 5\text{--}6 \mu\text{m}$ were formed when the magnesium-rich filler Al-4Mg-0.6Sc (samples 17–19) was used. Hot cracks and lacks of fusion occurred particularly in the weld seams produced with filler alloys EN AW 5183 and EN AW 5087. As a distinctive example, Figure 9(a) shows the joint cross section of sample 08, where no bonding between the steel sheet and the weld seam exists at the top section of the joint. The microstructure details of Figures 9(b) through (e) illustrate that a crack of varying width runs transversely through the IM layer. This type of cracking is

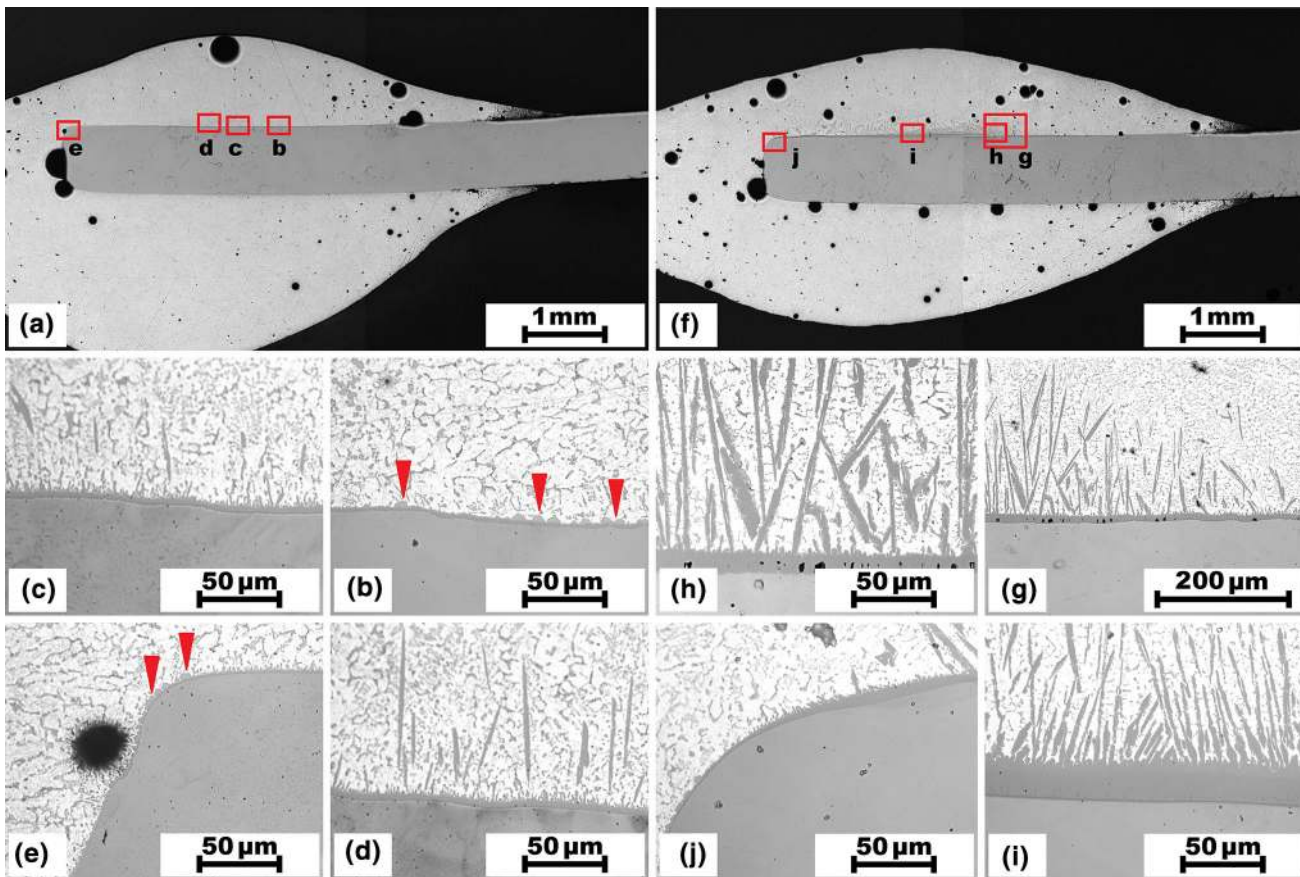


Fig. 8—Merged optical micrographs of the joint cross sections of sample 14 (a) and sample 16 (f). The details show small polyhedral particles marked with arrows (b), (e); isolated needle-shaped particles (c), (d); and dense clusters of large needle-shaped particles (g) through (j).

assumed to result from weld bead shrinkage due to solidification, which detaches fractions of the comparatively brittle IM layer from the surface of the steel sheet. It is also obvious that cracking is initiated near the weld seam surface, because the crack width tends to decrease from the surface of the weld, Figure 9(b), toward the cutting edge of the steel sheet, Figure 9(e).

As exemplarily shown in Figure 10(a) for sample 20, cracking is initiated at the zinc-rich region located at the base corner of the weld seam where just a very thin discontinuous IM layer has been formed. With ongoing solidification, the crack propagates then almost parallel to the interface between the weld seam and the steel sheet. The qualitative SEM-EDX line scan visualized in Figure 10(b) demonstrates that the contents of aluminum and iron markedly decrease, whereas the content of zinc increases, as shown in Figure 10(c). Since other zinc sources were not present, zinc accumulated in the corner region must originate from the coating of the steel sheet, which melted during welding. This coating is mandatory for the CMT process, because it ensures sufficient wettability of the steel sheet for liquid aluminum.^[55,74] However, evaporation of zinc may destabilize the welding process.^[75]

Remarkable effects of scandium (Sc) and zirconium (Zr) on reducing the IM layer thickness were not

observed. When using scandium-containing fillers, medium IM layers of $\bar{x} \approx 5\text{--}6\ \mu\text{m}$ (samples 17–19) and comparatively thick IM layers of $\bar{x} \approx 7\text{--}8\ \mu\text{m}$ (samples 20 and 22) were formed. However, the investigations revealed that the filler alloys Al-0.3Mg-0.5Sc-0.4Zr (sample 20) and Al-0.3Mg-0.4Sc-0.3Zr (sample 22) improve the hot-cracking resistance of the welds.^[68] This also explains why cracking of the IM layer was observed when using the scandium-free commercial filler alloys EN AW 5183 and EN AW 5087 (samples 05–10), but not when using scandium-containing filler alloy Al-4Mg-0.6Sc, although the Mg contents were similar. Hence, scandium does not decrease the thickness, but it indirectly reduces the hot-cracking tendency of the IM layer. In fact, this results from the scandium-induced grain refinement, which improves feeding of the weld bead during solidification and therefore reduces shrinkage tensions causing weld bead or IM layer cracking, respectively.

D. Influences of the Torch Type and the Torch–Workpiece Distance

The small differences of $\Delta\bar{x} < 1\ \mu\text{m}$ between the light gray and the medium gray bars shown in Figure 7 indicate that the distance between the torch and the

workpiece had just a minor influence on the layer thickness. The CMT Braze+ torch position 12 mm apart from the workpiece (samples 06, 10, 11, 15, and 18) caused the comparatively thinnest IM layer, but the torch position 6 mm apart from the workpiece (samples 05, 09, 12, 14, and 17) seems to be generally more favorable for achieving smooth welds, independent of the filler alloy used. The thickest IM layers of $\bar{x} > 10 \mu\text{m}$

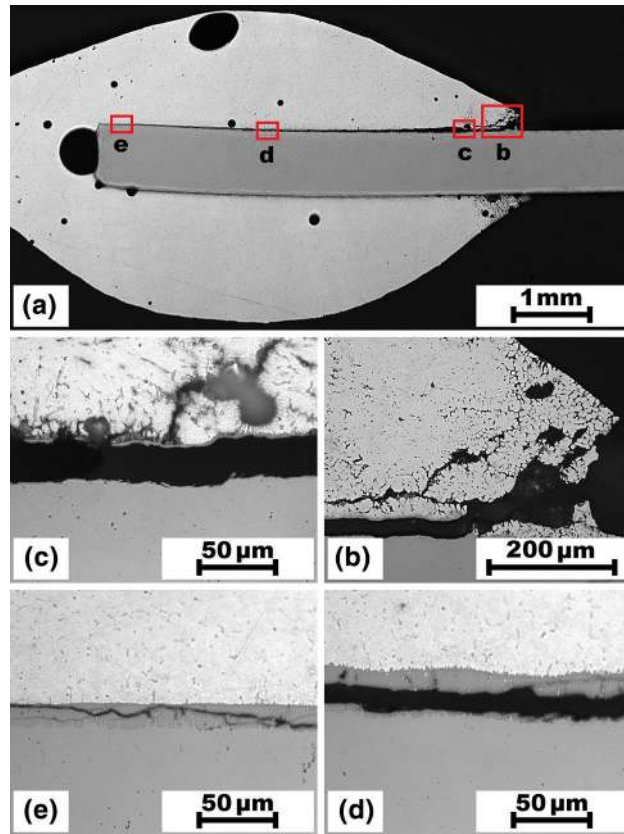


Fig. 9—Merged optical micrograph of the joint cross section of sample 08 (a). The details (b) through (e) show sections of a long crack which is initiated at the surface at the base corner of the weld (b) and which runs transversely through the IM layer toward the cutting edge of the steel sheet (e).

were formed when the Robacta500 torch was utilized for welding (samples 07 and 08). The influence of the torch type was even more pronounced when using filler Al-3Si-1Mn. As stated before, and as shown in Figure 8, IM layers of $\bar{x} < 4 \mu\text{m}$ and predominantly polyhedral particles were obtained with the CMT Braze+ torch (samples 14 and 15). In contrast, \bar{x} was approximately twice as thick, and long needle-shaped particles formed with the Robacta500 torch (sample 16). Thus, the CMT Braze+ torch was more favorable than the Robacta500 torch with regard to both limiting the IM layer thickness as well as preventing needle-shaped particles. Compared with the standard nozzle of the Robacta500 torch, the narrow conical nozzle of the CMT Braze+ torch increases the emerging speed of the shielding gas, which constricts the arc and improves cooling.^[12] Therefore, it seems that the different morphologies of faceted silicon-containing particles next to the IM layer are mainly triggered by the actual cooling conditions: more intense cooling promotes the formation of the polyhedral instead of the needle-shaped particles, particularly if silicon-rich filler alloys are used for welding.

The mean sectional IM layer thicknesses \bar{x}_{top} , \bar{x}_{side} , and \bar{x}_{bottom} determined for samples 05-22 are shown in Figure 11. In most samples, the layer at the top section of the bonding interface, *i.e.*, close to the welding torch, was distinctly thicker than that at the side or at the bottom sections of the bonding interface. A comparison of the widths of the error bars in Figure 11 indicates a generally more irregular IM layer at the top section than that at the side or at the bottom sections. From the position where the torch was located, the IM layer thickness tends to decrease bidirectionally: toward the cutting edge of the steel sheet as well as toward the base corner of the weld. Obviously, the majority of the filler alloy was deposited beneath the torch where the base materials were exposed to the highest thermal power and where the weld bead cooling was comparatively slow. Both these effects, intense heat input as well as decelerated cooling, promote the local growth of the IM layer and the formation of needle-shaped IM particles in sample 16. This corresponds to fundamental diffusion kinetics^[69] and to previous CMT experiments considering different heat inputs.^[70,71]

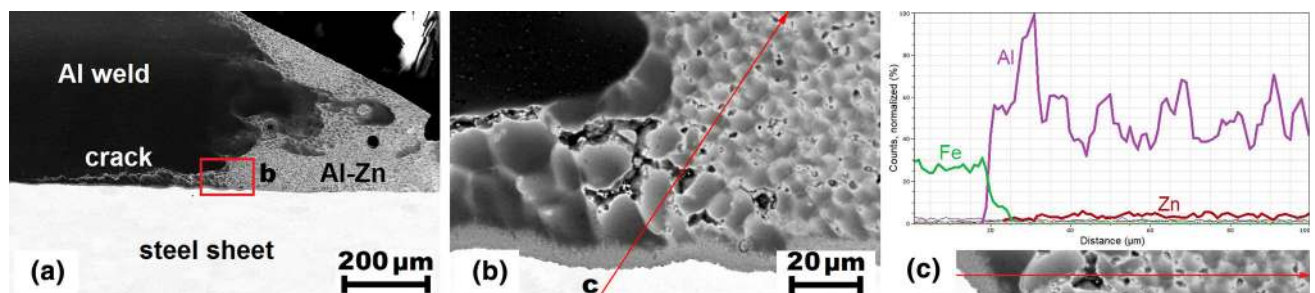


Fig. 10—Details of sample 20 captured with the SEM. Crack emerging from the zinc-rich region at the base corner of the weld (a), position of the SEM-EDX line scan at the location of crack initiation (b), and qualitative line scan graphs redrawn for Al, Fe, and Zn (c).

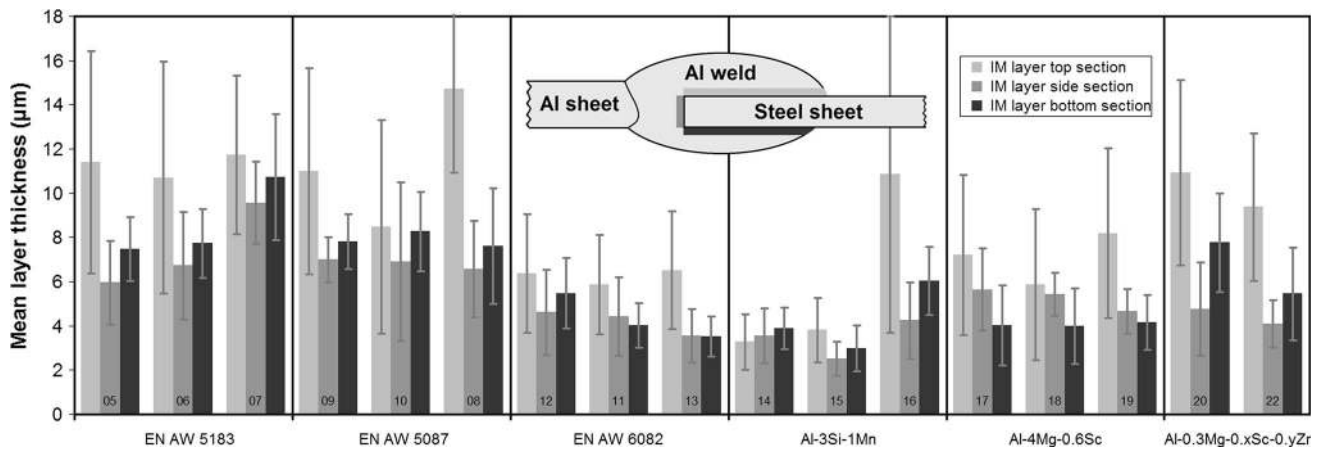


Fig. 11—Mean thicknesses of the IM layer determined for samples 05-22 at different sections (top, side, bottom) of the bonding interface.

IV. CONCLUSIONS

The current experimental study investigates the influences of different aluminum-based filler alloys and process parameters on the formation of the intermetallic (IM) layer for single-sided Cold Metal Transfer (CMT) welding of aluminum alloy EN AW 6014 T4 with galvanized steel HCT 450 X + ZE 75/75. According to the obtained results, the following conclusions are drawn:

- (1) Sheets of the aluminum alloy and the dual-phase steel are successfully butt welded with the single-sided CMT process. The blanks are fully penetrated by the weld seam, and the weld surface is free from spatter. Bonding between the weld seam and the steel sheet is achieved by the formation of an IM layer.
- (2) The composition of the filler alloy is the most important parameter influencing the IM layer thickness. The mean thickness reduces significantly by more than half when fillers with comparatively high silicon contents, *e.g.*, Al-3Si-1Mn, are used instead of fillers with high magnesium contents, *e.g.*, EN AW 5183 or EN AW 5087. For both of these Al-Mg filler alloys, severe cracking of the IM layer is observed, but not for filler alloy Al-4Mg-0.6Sc, although the magnesium contents are similar. Thus, it seems that scandium which is known to reduce cracking of the weld seam also prevents cracking of the IM layer.
- (3) The thinnest IM layer (mean thickness $< 4 \mu\text{m}$) without internal cracks was achieved with the Al-3Si-1Mn filler alloy. However, this filler alloy facilitates the formation of needle-like phases close to the bonding interface, which may deteriorate the properties of the joints, particularly their ductility and formability. Although they are relevant for the processing and application capabilities of the weldments, determining these properties is beyond the scope of the current article which primarily focuses on the welding process and on the weldability.
- (4) Both the increase in the heat input, *e.g.*, due to higher welding current and/or voltage, and the decrease in the cooling intensity principally tend to increase the thickness of the IM layer, since diffusion processes governing the layer formation are promoted at elevated temperatures.
- (5) The thickness of the IM layer shows spatial variations along the bonding interface between the weld seam and the steel sheet. The layer which forms at the top section of the interface, *i.e.*, which is located beneath the welding torch, is rather thicker than the layers which form at the side or at the bottom sections. When comparing the mean layer thicknesses at different sections of the bonding interface, they may vary up to a factor of about 2.
- (6) Particularly with regard to the reduction of the IM layer thickness, the CMT Braze+ torch is more favorable than the Robacta500 torch, whereas the influence of the distance between the torch and the workpiece, 6 or 12 mm, is more or less negligible. However, positioning the torch closer to the workpiece tends to improve the surface quality of the weld seam.
- (7) The current study focuses on technological aspects which are of practical interest in the design of dissimilar aluminum-steel welding processes, particularly in filler materials engineering. However, to improve the basic understanding on different alloying elements influencing the IM layer growth, detailed fundamental research into the atomic processes at the aluminum-steel interface during solidification is still necessary.

ACKNOWLEDGMENT

Open access funding provided by Graz University of Technology. The authors would like to thank the Austrian Research Promotion Agency (FFG) for the financial support of this study.

OPEN ACCESS

This article is distributed under the terms of the Creative Commons Attribution 4.0 International License (<http://creativecommons.org/licenses/by/4.0/>), which permits unrestricted use, distribution, and reproduction in any medium, provided you give appropriate credit to the original author(s) and the source, provide a link to the Creative Commons license, and indicate if changes were made.

REFERENCES

1. S. Oliver, T.B. Jones, and G. Fourlaris: *Mater. Sci. Technol.*, 2007, vol. 23 (4), pp. 423–31.
2. B.C. De Cooman, O. Kwon, and K.G. Chin: *Mater. Sci. Technol.*, 2012, vol. 28 (5), pp. 513–27.
3. W.S. Miller, L. Zhuang, J. Bottema, A.J. Wittebrood, P. De Smet, A. Haszler, and A. Vierregge: *Mater. Sci. Eng. A*, 2000, vol. 280, pp. 37–49.
4. J. Hirsch: *Mater. Trans.*, 2011, vol. 52 (5), pp. 818–24.
5. J.E. Gould: *Weld. J.*, 2012, vol. 91 (1), pp. 23–34.
6. U. Dilthey and L. Stein: *Sci. Technol. Weld. Join.*, 2006, vol. 11 (2), pp. 135–42.
7. T. Sakiyama, Y. Naito, Y. Miyazaki, T. Nose, G. Murayama, K. Saita, and H. Oikawa: *Nippon Steel Techn. Rep.*, 2013, vol. 103, pp. 91–97.
8. G. Meschut, M. Matzke, R. Hoerhold, and T. Olfemann: *Procedia CIRP*, 2014, vol. 23, pp. 19–23.
9. ASM Handbook: *Volume 6: Welding, Brazing and Soldering*, ASM International, Materials Park, OH, 1993.
10. D.R.G. Achar, J. Ruge, and S. Sundaresan: *Aluminium*, 1980, vol. 56 (2), pp. 147–49; (3), pp. 220–23; (4), pp. 291–93.
11. M. Mazar Atabaki, M. Nikodinovski, P. Chenier, J. Ma, M. Harooni, and R. Kovacevic: *J. Manuf. Sci. Prod.*, 2014, vol. 14 (2), pp. 59–78.
12. Fronius International GmbH: Cold Metal Transfer - The Technology, 2011, <http://www.fronius.com/>.
13. C.G. Pickin and K. Young: *Sci. Technol. Weld. Join.*, 2006, vol. 11 (5), pp. 583–85.
14. C.G. Pickin, S.W. Williams, and M. Lunt: *J. Mater. Process. Technol.*, 2011, vol. 211, pp. 496–502.
15. J. Feng, H. Zhang, and P. He: *Mater. Design*, 2009, vol. 30, pp. 1850–52.
16. H. Pinto, A. Pyzalla, H. Hackl, and J. Bruckner: *Mater. Sci. Forum*, 2006, vols. 524–525, pp. 627–32.
17. L. Agudo, S. Weber, H. Pinto, E. Arenholz, J. Wagner, H. Hackl, J. Bruckner, and A. Pyzalla: *Mater. Sci. Forum*, 2008, vols. 571–572, pp. 347–53.
18. L. Agudo Jácome, N. Jank, and J. Wagner: *Steel Res Int.*, 2008, vol. 79 (7), pp. 530–35.
19. L. Agudo Jácome, S. Weber, A. Leitner, E. Arenholz, J. Bruckner, H. Hackl, and A.R. Pyzalla: *Adv. Eng. Mater.*, 2009, vol. 11 (5), pp. 350–58.
20. J. Bruckner: *Weld. J.*, 2005, vol. 84 (6), pp. 38–40.
21. L. Agudo, D. Eyidi, C.H. Schmaranzer, E. Arenholz, N. Jank, J. Bruckner, and A.R. Pyzalla: *J. Mater. Sci.*, 2007, vol. 42 (12), pp. 4205–14.
22. H.T. Zhang, J.C. Feng, P. He, and H. Hackl: *Mater. Charact.*, 2007, vol. 58, pp. 588–92.
23. H.T. Zhang, J.C. Feng, and P. He: *Mater. Sci. Technol.*, 2008, vol. 24 (11), pp. 1346–49.
24. H.T. Zhang, J.C. Feng, P. He, B.B. Zhang, J.M. Chen, and L. Wang: *Mater. Sci. Eng. A*, 2009, vol. 499, pp. 111–13.
25. S. Yang, J. Zhang, J. Lian, and Y. Lei: *Mater. Design*, 2013, vol. 49, pp. 602–12.
26. R. Cao, J.H. Sun, J.H. Chen, and P. Wang: *J. Manuf. Sci. Eng.*, 2014, vol. 136 (5), pp. 051015–1–10.
27. S. Madhavan, M. Kamaraj, and L. Vijayaraghavan: *Sci. Technol. Weld. Join.*, 2016, vol. 21 (3), pp. 194–200.
28. S. Niu, S. Chen, H. Dong, D. Zhao, X. Zhang, X. Guo, and G. Wang: *J. Mater. Eng. Perform.*, 2016, vol. 25, pp. 1839–47.
29. E. Ünel and E. Taban: *Weld. World*, 2017, vol. 61, pp. 1–9.
30. R. Cao, Q. Huang, J.H. Chen, and P. Wang: *J. Alloy. Compd.*, 2014, vol. 585, pp. 622–32.
31. H. Lei, Y. Li, B.E. Carlson, and Z. Lin: *J. Manuf. Sci. Eng.*, 2015, vol. 137 (10), pp. 051028–1–10.
32. H. Lei, Y. Li, B.E. Carlson, and Z. Lin: *J. Manuf. Sci. Eng.*, 2016, vol. 138 (7), pp. 071009–1–13.
33. V.R. Ryabov: *Fusion Welding of Aluminum to Steel*, Edited Machine Translation of the USAF Foreign Technology Division, National Technical Information Service, US Department of Commerce, Springfield, VA, 1973.
34. N. Jank, H. Stauffer, and J. Bruckner: *BHM*, 2008, vol. 153 (5), pp. 189–92.
35. U.R. Kattner and B.P. Burton: *ASM Handbook, Volume 3: Alloy Phase Diagrams*, ASM International, Materials Park, OH, 1992.
36. E. Gebhardt and W. Obrowski: *Z. Metallk.*, 1953, vol. 44, pp. 154–60.
37. T. Heumann and S. Dittrich: *Z. Metallk.*, 1959, vol. 50, pp. 617–25.
38. S. Kobayashi and T. Yakou: *Mater. Sci. Eng. A*, 2002, vol. 338, pp. 44–53.
39. G. Eggeler, H. Vogel, J. Friedrich, and H. Kaesche: *Pract. Metallogr.*, 1985, vol. 22, pp. 163–70.
40. G. Eggeler, W. Auer, and H. Kaesche: *J. Mater. Sci.*, 1986, vol. 21, pp. 3348–50.
41. V.I. Dybkov: *J. Mater. Sci.*, 1990, vol. 25, pp. 3615–33.
42. A. Bahadur and O.N. Mohanty: *Mater. Trans. JIM*, 1991, vol. 32 (11), pp. 1053–61.
43. A. Bahadur and O.N. Mohanty: *Mater. Trans. JIM*, 1995, vol. 36 (9), pp. 1170–75.
44. A. Shyam, S. Suwas, and S. Bhargava: *Pract. Metallogr.*, 1997, vol. 34, pp. 264–77.
45. K. Bouché, F. Barbier, and A. Coulet: *Mater. Sci. Eng. A*, 1998, vol. 249, pp. 167–75.
46. H.R. Shahverdi, M.R. Ghomashchi, S. Shabestari, and J. Hejazi: *J. Mater. Process. Technol.*, 2002, vol. 124, pp. 345–52.
47. A. Bouayad, C. Gerometta, A. Belkebir, and A. Ambari: *Mater. Sci. Eng. A*, 2003, vol. 363, pp. 53–61.
48. W.-J. Cheng and C.-J. Wang: *Surf. Coat. Technol.*, 2009, vol. 204, pp. 824–28.
49. Y. Tanaka and M. Kajihara: *Mater. Trans.*, 2009, vol. 50 (9), pp. 2212–20.
50. Y. Tanaka and M. Kajihara: *J. Mater. Sci.*, 2010, vol. 45, pp. 5676–84.
51. H. Springer, A. Kostka, E.J. Payton, D. Raabe, A. Kaysser-Pyzalla, and G. Eggeler: *Acta Mater.*, 2011, vol. 59, pp. 1586–1600.
52. F. Yin, M. Zhao, Y. Liu, W. Han, and Z. Li: *T. Nonferr. Met. Soc. China*, 2013, vol. 23, pp. 556–61.
53. N. Takata, M. Nishimoto, S. Kobayashi, and M. Takeyama: *Intermet.*, 2014, vol. 54, pp. 136–42.
54. N. Takata, M. Nishimoto, S. Kobayashi, and M. Takeyama: *ISIJ Int.*, 2015, vol. 55 (7), pp. 1454–59.
55. H. Springer, A. Szczepaniak, and D. Raabe: *Acta Mater.*, 2015, vol. 96, pp. 203–11.
56. M.V. Akdeniz and A.O. Mekhrabov: *Acta Mater.*, 1998, vol. 46 (4), pp. 1185–92.
57. J.L. Song, S.B. Lin, C.L. Yang, and C.L. Fan: *J. Alloy. Compd.*, 2009, vol. 488, pp. 217–22.
58. B. Götzinger, W. Karner, M. Hartmann, and Z. Silveyeh: *Lightweight Des.*, 2017, vol. 10 (2), pp. 50–55.
59. European Steel and Alloy Grades / Numbers Searchable Database (National Technical University Kharkiv Polytechnic Institute, 2016), <http://www.steelnumber.com/>.
60. B. Irving: *Weld. J.*, 1997, vol. 76 (7), pp. 53–57.
61. A.F. Norman, P.B. Prangnell, and R.S. McEwen: *Acta Mater.*, 1998, vol. 46 (16), pp. 5715–32.
62. V.V. Zakharov: *Met. Sci. Heat Treat.*, 2003, vol. 45 (7–8), pp. 246–53.
63. Z. Ahmad: *JOM*, 2003, vol. 55 (2), pp. 35–39.
64. J. Røystad and N. Ryum: *Int. Mater. Rev.*, 2005, vol. 50 (1), pp. 19–44.

65. M.G. Mousavi, C.E. Cross, and Ø. Grong: *Sci. Technol. Weld. Join.*, 1999, vol. 4 (6), pp. 381–88.
66. A.F. Norman, S.S. Birley, and P.B. Prangnell: *Sci. Technol. Weld. Join.*, 2003, vol. 8 (4), pp. 235–45.
67. A.F. Norman, K. Hyde, F. Costello, S. Thompson, S. Birley, and P.B. Prangnell: *Mater. Sci. Eng. A*, 2003, vol. 354, pp. 188–98.
68. Z. Silvayeh, R. Vallant, C. Sommitsch, B. Götzinger, and W. Karner: In: *Proc. 10th Int. Conf. Trends Weld. Res.*, October 11-14, 2016, Tokyo, pp. 32-35.
69. H. Mehrer: *Diffusion in Solids*, Springer, Berlin-Heidelberg-New York, 2007.
70. S. Madhavan, M. Kamaraj, L. Vijayaraghavan, and K. Srinivasa Rao: *Mater. Sci. Technol.*, 2017, vol. 33 (2), pp. 200–09.
71. B. Mezrag, F. Deschaux-Beaume, and M. Benachour: *Sci. Technol. Weld. Join.*, 2015, vol. 20 (3), pp. 189–98.
72. S.P. Gupta: *Mater. Charact.*, 2003, vol. 49, pp. 269–91.
73. T. Maitra and S.P. Gupta: *Mater. Charact.*, 2003, vol. 49, pp. 293–311.
74. M. Gatzen, T. Radel, C. Thomy, and F. Vollertsen: *J. Mater. Process. Technol.*, 2014, vol. 214, pp. 123–31.
75. Q. Lin, G. Mao, Q. Huang, R. Cao, and J. Chen: *J. Iron Steel Res.*, 2016, vol. 23 (6), pp. 566–72.